HAL
open science

Numerical Airframe Aerodynamic Performance Prediction: An Exergy Point of View.

A. Arntz, O. Atinault, D. Destarac

To cite this version:

A. Arntz, O. Atinault, D. Destarac. Numerical Airframe Aerodynamic Performance Prediction: An Exergy Point of View.. 49th International Symposium of Applied Aerodynamics, Mar 2014, LILLE, France. hal-01059075

HAL Id: hal-01059075

https://onera.hal.science/hal-01059075

Submitted on 29 Aug 2014

HAL is a multi-disciplinary open access archive for the deposit and dissemination of scientific research documents, whether they are published or not. The documents may come from teaching and research institutions in France or abroad, or from public or private research centers.

L'archive ouverte pluridisciplinaire **HAL**, est destinée au dépôt et à la diffusion de documents scientifiques de niveau recherche, publiés ou non, émanant des établissements d'enseignement et de recherche français ou étrangers, des laboratoires publics ou privés.

49th International Symposium of Applied Aerodynamics
Lille, 24-25-26 March 2014

FP04-2014-arntz

Numerical Airframe Aerodynamic Performance Prediction: An Exergy Point of View

Aurélien Arntz, Olivier Atinault, Daniel Destarac

ONERA – The French Aerospace Lab, 92190 Meudon, FRANCE
aurelien.arntz@onera.fr, olivier.atinault@onera.fr, daniel.destarac@onera.fr

ABSTRACT

The prediction of the aerodynamic performance of airframe has been historically made *via* the determination and decomposition of the force opposing the aircraft motion: drag.
The paper presents an innovative energy approach which is based on the destruction of exergy by irreversible processes. The design that destroys the less exergy is the most efficient one.
A required step in the development process is to validate its numerical implementation *via* various CFD test cases: 2D airfoil and 3D wing RANS test cases are presented in subsonic and transonic regimes. Mesh convergence studies prove the exergy approach to have a similar accuracy as the traditional near-field drag approach while offering a phenomenological breakdown comparable to a far-field formulation.

INTRODUCTION

A sustainable growth of aviation requires the development of more advanced aircraft to reduce fuel consumption, noise and pollutant emissions. Typical breakthrough concepts include blended-wing-bodies with distributed propulsion systems ingesting a portion of the boundary layer of the airframe. One of the most promising configurations may be the NASA N3-X concept (Fig. 1) which decouples the power producing parts of the system from the thrust producing parts of the system, allowing each to be optimized for its respective task [1]. This kind of promising aircraft requires the development of methodologies and tools enabling its preliminary design.

Figure 1: NASA N3-X BWB Concept

ONERA is developing an innovative formulation that is especially suitable for the design of complex blended-wing-bodies with boundary layer ingestion. The approach is based on the evaluation of *exergy* which, in the perspective of producing mechanical work, is defined as the *useful* part of energy, as opposed to *anergy* which is the part that can never be transformed into work. This approach is based on the work of Sadi Carnot on heat engines from which he stated that the conversion of thermal energy into mechanical work can only be achieved through an efficiency lower than unity. The exergy analysis is gaining interest in the aerospace community as providing a system-level approach for the design of complex aerospace vehicles.

1. THEORETICAL FORMULATION

The analysis consists in identifying a far-field drag expression in the outflow of total enthalpy on one hand, and to introduce the second law of thermodynamics to decompose the anergy outflow into physical phenomena on the other hand. The derivation presented is restricted to steady flows without energy addition, neither thermal nor mechanical, but its extension to powered configurations has been initiated.

1.1. Control Volume

The analysis is made in a continuous volume surrounding the body under study. The control volume is delimited by the aircraft surface, a surface excluding any discontinuous shock wave and an outer boundary. The latter is chosen so that the upstream and lateral surfaces are pushed far from the body and the downstream surface is a plane perpendicular to the freestream located at a fixed distance downstream, see Fig. 2.

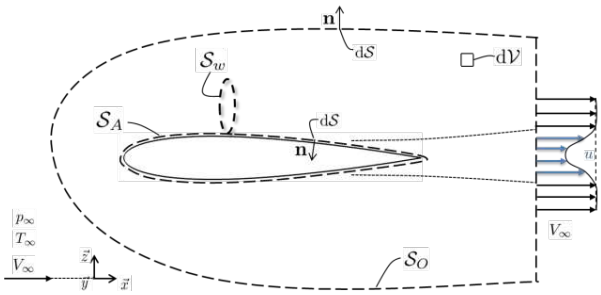

Figure 2 : Control volume representation.

The derivation consists in applying fundamental principles to the fluid under study, namely the conservation of mass, the momentum relation, as well as the first and second law of thermodynamics. We consider the fluid as a perfect gas.

1.2. Mass Conservation

In local and divergence form, the time-averaged mass conservation reads:

$$\nabla \cdot \left(\rho \vec{V}\right) = 0 \qquad (1)$$

Integration within the control volume and use of the divergence theorem yields:

$$\int_{S_O} \rho \left(\vec{V} \cdot \vec{n}\right) dS = 0 \qquad (2)$$

This relation is used later in the development to simplify the equations.

1.3. Momentum Relation

In local and divergence form, the time-averaged *x*-momentum relation reads:

$$\nabla \cdot \left(\rho u \vec{V}\right) = -\frac{\partial p}{\partial x} + \nabla \cdot \vec{\tau_x} \qquad (3)$$

Again, integration within the control volume and use of the divergence theorem yields the theoretical equivalence between the near-field drag and far-field drag:

$$D_p + D_f = -\int_{S_O} \left[\rho\, u \left(\vec{V} \cdot \vec{n}\right) + (p - p_\infty) n_x\right] dS \qquad (4)$$

where D_p and D_f are respectively the pressure drag and the friction drag, forming the near-field drag. The right-hand side integral is a far-field expression of drag which constitutes the starting point of any far-field drag formulation. The viscous forces have been neglected as they rapidly vanish a few body lengths downstream of the body. It is this latter term that will be identified in the outflow of total enthalpy.

1.4. Exergy Analysis

The exergy analysis is based on the evaluation of the specific flow exergy:

$$\varepsilon = (h_i - h_{i_\infty}) - T_\infty (s - s_\infty) \qquad (5)$$

where h_i is the total enthalpy, s the entropy, and the subscript ∞ denotes reference conditions.

The time-averaged change in exergy can be expressed locally as:

$$\nabla \cdot \left(\rho \varepsilon \vec{V}\right) = \nabla \cdot \left(\rho \delta h_i \vec{V}\right) - T_\infty \nabla \cdot \left(\rho \delta s \vec{V}\right) \qquad (6)$$

The derivation consists in evaluating the outflow of exergy through the outer boundary. Introduction of the first and second laws of thermodynamics allows breaking down the right-hand side terms of Eq. (4) into physical phenomena of interest.

1.4.1. Energy Relation

The relative total enthalpy can be decomposed as:

$$\nabla \cdot \left(\rho \delta h_i \vec{V}\right) = \nabla \cdot \left(\rho \delta e \vec{V}\right) + p_\infty \nabla \cdot \vec{V} + \nabla \cdot (p - p_\infty)\vec{V} + \nabla \cdot \left(\tfrac{1}{2} \rho V^2 \vec{V}\right) \qquad (7)$$

where $p_\infty \nabla \cdot \vec{V}$ has been added and subtracted. Considering the total enthalpy outflow to be zero according to the first law, we integrate Eq. (7) within the control volume and apply the divergence theorem to get:

$$\boxed{0 = -\mathrm{DV}_\infty + \dot{E}_u + \dot{E}_v + \dot{E}_p + \dot{E}_{th} + \dot{E}_W \qquad (8)}$$

where we have used the mass conservation. The terms introduced are defined hereafter:

- $\mathrm{DV}_\infty = \mathrm{V}_\infty \int_{S_O} \left[\rho\, u \left(\vec{V} \cdot \vec{n}\right) + (p - p_\infty) n_x\right] dS$
  Is the power of the far-field drag, see Eq. (4).

- $\dot{E}_u = \int_{S_O} \rho\, u^2 \left(\vec{V} \cdot \vec{n}\right) dS$ (10)

  is the streamwise kinetic energy deposition rate and is generally attributed to wakes.
- $\dot{E}_v = \int_{S_O} \rho\, (v^2 + w^2) \left(\vec{V} \cdot \vec{n}\right) dS$ (11)

  is the transverse kinetic energy deposition rate and is mainly attributed to lift-induced vortices.
- $\dot{E}_p = \int_{S_O} (p - p_\infty) \left[(\vec{V} - \vec{V}_\infty) \cdot \vec{n}\right] dS$ (12)

  is the boundary pressure work rate and is associated to the two previously-described phenomena.
- $\dot{E}_{th} = \int_{S_O} \rho\, \delta e \left(\vec{V} \cdot \vec{n}\right) dS$ (13)

  is the rate of thermal energy outflow.
- $\dot{E}_W = \int_{S_O} p_\infty \left(\vec{V} \cdot \vec{n}\right) dS$ (14)

  is the rate of work that the systems performs by expanding to displace the ambient air at reference pressure.

1.4.2.Anergy Relation

Inserting the internal energy equation

$$\nabla \cdot \left(\rho \delta e \vec{V}\right) = -p \nabla \cdot \vec{V} + \bar{\bar{\tau}} \cdot \left(\nabla \cdot \vec{V}\right) - \nabla \cdot \vec{q} \qquad (15)$$

into the time-averaged Gibbs' equation,

$$\mathrm{T}\nabla \cdot \left(\rho \delta s \vec{V}\right) = \nabla \cdot \left(\rho \delta e \vec{V}\right) + p \nabla \cdot \vec{V} \qquad (16)$$

one gets the rate of change of anergy expressed as:

$$T_\infty \nabla \cdot \left(\rho \delta s \vec{V}\right) = \frac{T_\infty}{T} \Phi + \frac{T_\infty}{T^2} k\, \nabla T^2 - \nabla \cdot \frac{T_\infty}{T} \vec{q} \qquad (17)$$

where $\Phi = \bar{\bar{\tau}} \cdot \left(\nabla \cdot \vec{V}\right)$ is the viscous dissipation, k the fluid thermal conductivity and $\vec{q}$ is the heat flux by conduction expressed using the Fourier law $\vec{q} = -k \nabla T$.

Integration of Eq. (17) within the control volume and use of the divergence theorem, one gets:

$$\boxed{\dot{A} = \dot{A}_\Phi + \dot{A}_{\nabla T} + \dot{A}_\mathrm{w} \qquad (18)}$$

where we considered adiabatic surfaces and neglected the heat flux across the outer boundary.

The terms introduced are defined next:

- $\dot{A} = T_\infty \int_{S_O} \rho\, \delta s \left(\vec{V} \cdot \vec{n}\right) dS$ (19)

  is the rate of total anergy outflow and represents all irreversibilities that have occurred within the control volume.
- $\dot{A}_\Phi = \int_V \frac{T_\infty}{T} \Phi\, dV$ (20)

  is the rate of anergy generation by viscous dissipation which converts kinetic energy into thermal energy. This process tends to form a uniform field of velocity and pressure in which the system is back in mechanical equilibrium with its surroundings.
- $\dot{A}_{\nabla T} = \int_V \frac{T_\infty}{T^2} k\, \nabla T^2\, dV$ (21)

  is the rate of anergy generation by thermal mixing which reduces any differences in temperature in the flow field. This process therefore tends to form a uniform field of temperature in which the system is in thermal equilibrium with its surroundings.
- $\dot{A}_\mathrm{w} = T_\infty \int_{S_w} -\rho\, \delta s \left(\vec{V} \cdot \vec{n}\right) dS$ (22)

  is the rate of anergy generation by shock waves whose process converts mechanical energy into thermal energy.

Note that the viscous dissipation is a function of the square of velocity gradients.

1.4.3.Exergy Relation

We now form the rate of exergy outflow by subtracting Eq. (18) from Eq. (8) and isolate DV_∞:

$$\boxed{\mathrm{DV}_\infty = \dot{E}_{tot} + \dot{\mathfrak{E}}_{th} + \dot{A}_\Phi + \dot{A}_{\nabla T} + \dot{A}_\mathrm{w} \qquad (23)}$$

where the terms are defined hereafter:

- $\dot{E}_{tot} = \dot{E}_u + \dot{E}_v + \dot{E}_p$ (24)

  is the rate of net mechanical energy outflow.
- $\dot{\mathfrak{E}}_{th} = \dot{E}_{th} + \dot{E}_W - \dot{A}$ (25)

  is the rate of thermal exergy outflow, which represents the amount of useful work that could be extracted from the thermal energy.

Physically speaking, considering a fixed body with an incoming flow as in wind tunnel testing, the following energy-based interpretation of Eq. (23) can be suggested. The incoming flow has a certain exergy due to its velocity with reference to the fixed body reference frame.

As the flow passes in the vicinity of the obstacle, boundary layers develop and slow the fluid down. This reduction in velocity means that a portion of the exergy of the flow is destroyed. According to the first law, the loss in kinetic energy appears as a gain in thermal energy. Then, the thermal mixing dissipates any temperature difference, destroying any potential for work extraction from the thermal energy.

The exergy analysis redefines the aerodynamic loss as irreversible phenomena. The design that destroys the less exergy is the most efficient one.

2. NUMERICAL CONSIDERATIONS

The paper presents application of the formulation to various unpowered airframe CFD flow solutions that have been performed on structured meshes with the ONERA-elsA Navier-Stokes solver [2]. This software is here used with a cell-centred finite-volume discretization and time integration is carried out by a backward Euler scheme with implicit LU-SSOR relaxation. Spatial discretization is realized using a central Jameson scheme with artificial viscosity. Fully turbulent flows are modelled with the Spalart-Allmaras turbulence model.
In order to reach high levels of convergence, all computations were continued until a drag variation lower than 0.0001 drag count was observed over (at least) the last thousand iterations. When mesh refinement studies are provided, the same numerical settings have been used for all computations (CFL, multigrid techniques, etc.) in order to investigate only the effect of mesh density.

2.1. Numerical Implementation

The formulation has been implemented in an existing Fortran code dedicated to post-processing RANS and Euler flow solutions (*ffd72*). The cell-centered conservative variables are extracted from the CFD flow solution along with grid and other numerical information. The quantities that are required for the formulation are then calculated (p, T, ∇p, ∇T, etc). Face-based management implies that gradients are calculated at cell interface by simple averaging.
The post-processing time is generally in the order of a few seconds to a few minutes depending on the grid density.
Numerically speaking the lateral and upstream surfaces of the control volume are pushed to the mesh boundaries.

2.2. Discontinuous Shock Wave Treatment

The rate of anergy generation by shock waves can be determined *via* the *direct method* (proposed above) by relying on the definition of the surface enclosing the discontinuous shock waves:

$$\dot{A}_w^d = T_\infty \int_{S_w} -\rho\, \delta s \left(\vec{V} \cdot \vec{n}\right) dS \qquad (26)$$

Numerically speaking, the definition of S_w can be achieved through shock detector as proposed by Tognaccini [3]:

$$\lambda_c = \frac{\vec{V} \cdot \overrightarrow{\nabla p}}{a \left| \overrightarrow{\nabla p} \right|} \qquad (27)$$

where *a* is the local speed of sound. If $\lambda_c > 1$. the cell considered is counted in the volume delimited by the surface S_w. Because discontinuities may not be perfectly computed (on coarse meshes), additional cell layers are added. The number of layers that are required may differ from case to case but generally ranges from 3 to 6.

An alternative way of computing the rate of anergy generation by shock waves can be the evaluation of all three other terms of Eq. (18) in order to deduce the one associated to shocks:

$$\dot{A}_w^i = \dot{A} - \dot{A}_\Phi - \dot{A}_{\nabla T} \qquad (28)$$

This procedure will be referred to as *indirect method*. This choice is expected to have the drawback of taking into account spurious (non physical) phenomena.

2.3. Validation Method

In a direct analogy to the traditional drag counts, all terms of the exergy-based formulation can be non-dimensionalised with respect to the power of the freestream dynamic pressure to express *power counts*. For example for $\dot{E}_{tot}$:

$$C\dot{E}_{tot} = \frac{\dot{E}_{tot}}{0.5\, \rho_\infty\, V_\infty^3\, A_{ref}} \qquad (29)$$

where A_{ref} is the area of the reference surface of the body under study. By doing so, the magnitude of the power counts, abbreviated *pc,* is directly comparable to the more common drag counts, abbreviated *dc*. The sum of all right-hand side terms of Eq. (23) expressed in power counts, is written as CD_ε.

Exergy-based results are compared to the traditional near-field drag and to the far-field formulation of van der Vooren and Destarac [4]; the latter offering a phenomenological breakdown and a spurious drag identification.
Acceptable results will be considered if $CD_\varepsilon = CD_{nf} \pm 1\, dc/pc$. Numerical results are given on the last page of the paper.

3. 2D NACA 0012 AIRFOIL – RANS

This test case has been selected for its popularity and simple geometry. It will be used to investigate first a subsonic and viscous flow and then a transonic and viscous flow.

3.1. Grids & Numerics

An original NACA 0012 geometry was modified to get a sharp trailing edge and four monoblock-mesh densities were generated: 256 x 64, 512 x 128, 1024 x 256 and 2048 x 512. All meshes extend 150 chords in all directions (see Fig. 3) and provide $y^+ = 1$.

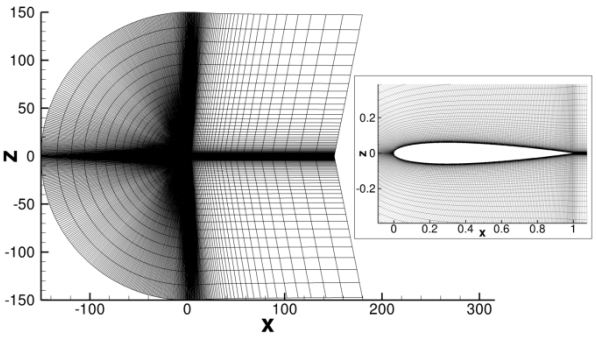

Figure 3 : 512 x 128 NACA 0012 grid.

Subsonic flows at M_∞=0.20 and transonic flows at M_∞=0.80 were computed at zero incidence and with $Re = 3\ 10^6$.
Fig. 4 gives an overview of the flow for the transonic regime. The top half shows the thermal mixing while the bottom half illustrates the anergy associated to viscous dissipation.

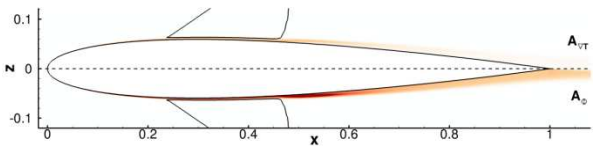

Figure 4 : 2D NACA 0012 Airfoil immersed in a viscous and transonic flow. Mesh: 512 x 128.

First, one can see that the two irreversible phenomena are well located within the boundary layers, as expected. Plotted on the same scale, it is clear that generation of viscous anergy is greater than the one associated to thermal mixing.

3.2. Mesh Convergence Study

Results of all three approaches are presented in Tables 1 for the subsonic flows. The downstream plane is located 2 chords downstream in both flow regimes in order to be able to neglect viscous forces in Eq. (4).

As regards subsonic performance prediction, we observe that a relatively large error is made on the coarsest mesh while acceptable results are to be found for the finer meshes. It is suggested that the gradients calculation is the origin of the discrepancy. As a greater number of cells are added in the grid, the gradient calculation becomes more accurate and therefore the exergy-based formulation converges towards the near-field value.

For the transonic flows, Tables 2 & 3 gives the results for the drag approaches and for the exergy-based formulation, respectively. Note that the downstream plane is also located 2 chords downstream. It appears that the shock surface determined to yield the best result required the addition of 6 cell layers, as shown in Fig. 5:

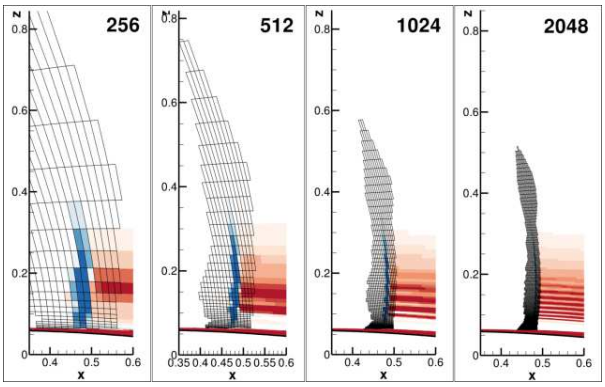

Figure 5 : Contours of entropy relative to freestream. Cells contained in the shock surface with grid refinement from left to right.

The performance prediction on coarse meshes is found highly sensitive on the choice of wave anergy calculation.

- The indirect method provides a total drag power in close agreement to the near-field approach. However, a detailed analysis reveals that the wave anergy is overpredicted and balances the deficit in viscous (and thermal) anergy; none of them being accurately predicted.
- The direct method has the advantage of providing a wave anergy close to the far-field drag formulation, but, by not balancing the viscous (and thermal) terms, yields a total drag power that is relatively far from the near-field approach.

Note that the two definitions converge towards the same value as the mesh is refined, as expected.
Although the thermal mixing was negligible at subsonic regimes, it corresponds to more than 10% of the anergy associated to viscous dissipation at transonic regimes.

3.3. Wake Analysis

For the both flow regimes, Fig. 6 illustrates the variation of the drag-power coefficient CD_ε when the downstream plane is moved aft from the body. This exergy-based coefficient has been non-dimensionalised by the near-field drag coefficient

CD_{nf} computed for each grid. The solid lines refer to the subsonic flows while the dashed lines refer to the transonic flows (with the direct method of wave anergy calculation). The location of the downstream plane used for obtaining the results presented in Tables 1 & 3 is highlighted in orange (xPlane = 3.).

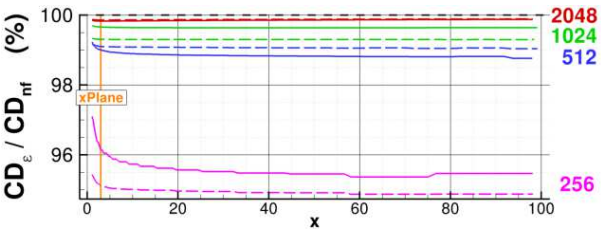

Figure 6 : Evolution of $CD_{\varepsilon}/\ CD_{nf}$ when the plane is moved downstream.

One can see that the total drag-power coefficient rapidly decreases a few chords downstream of the airfoil on the coarsest grids. This phenomenon can be explained by the failure of the gradient computation to effectively capture the wake dissipation. This rapid decrease in total drag-power disappears as mesh is refined and the coefficient becomes effectively independent on the control volume.
As the mechanical outflows are dissipated, there is a corresponding increase in viscous and thermal anergy, according to Eq. (22). It has been found that the dissipation of the wake accounts for about 13% of the total dissipation.

4. 3D ELLIPTICAL WING – EULER

This test case has been chosen to investigate the reversible formation of lift-induced vortices *via* a flow modelled by the Euler equations. We therefore consider a fluid that is both inviscid (μ=0) and calorically perfect (k=0). As a consequence, there is neither viscous dissipation nor thermal mixing. Also, as low-speed flows we consider no shock waves and Eq. (22) reduces to:

$$\mathrm{DV}_{\infty} = \dot{E}_u + \dot{E}_v + \dot{E}_p + \dot{\mathcal{E}}_{th} \qquad (30)$$

4.1. Grids & Numerics

The wing geometry is based on the NACA 0012 Airfoil and has been built so as to provide a theoretical elliptical (aerodynamic) loading. Three monoblock-grid densities have been generated by refining in each direction: 64 x 64 x 32, 128 x 128 x 64, 256 x 256 x 128. All meshes extend 150 chords in all directions as shown in Fig. 7 for the medium mesh density.

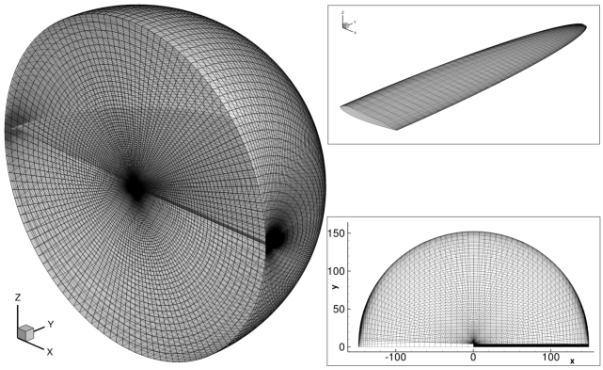

Figure 7 : 128 x 128 x 64 grid of a theoretically elliptically loaded wing.

Flows at M=0.20 have been computed with an incidence set at 6 degrees.

4.2. Flow Visualisation

Fig. 8 illustrates the transverse kinetic energy associated to the lift-induced vortex along with the pressure acting on the wing.

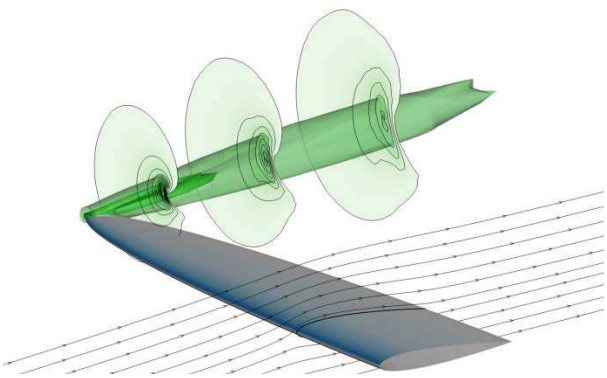

Figure 8 : 3D Wing Euler computation, medium mesh. Contours and iso-surface of transverse kinetic energy and pressure relative to freestream on the wing.

4.3. Mesh Convergence Study

For each grid, a reference drag coefficient is given and calculated as follows:

$$CD_{ref} = \frac{CL^2}{\pi\ AR} \qquad (31)$$

where CL is the lift coefficient and AR is the aspect ratio. As a result, we consider that the target drag coefficient depends on the lift coefficient and aspect ratio computed for each solution.

Results are to be found in Table 4 when the downstream plane is located 0.02 root chord downstream of the wing.

Note the great variations of near-field drag with mesh refinement as opposed to the much more precise far-field drag coefficient which is capable of determining non-negligible spurious phenomena. Very satisfactory results are provided by the exergy-based formulation whose precision outperforms the near-field approach. The low thermal exergy observed is mainly due to compressibility effects.

4.4. Wake Analysis

Fig. 9 illustrates all main terms of Eq. (30) when the outer boundary is moved downstream of the wing. The axial kinetic energy and transverse kinetic energy outflows are respectively represented as blue and green lines. The pressure-work rate is represented in orange while the total exergy-based drag power coefficient is given in red. Thermal exergy is represented in pink. Triangle, square and circle symbols refer respectively to the 64, 128 and 256 meshes.

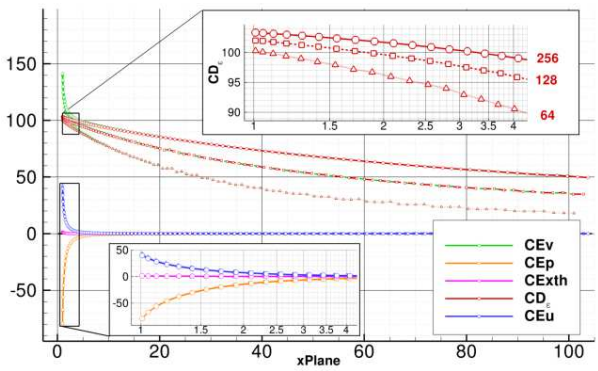

Figure 9 : Evolution of all terms of Eq. when the downstream plane is moved aft of the wing.

First, one can see that the total drag coefficient (red) reduces very rapidly to the transverse kinetic energy outflow (green) within a few body lengths. Thermal exergy is very negligible even directly downstream of the wing.
Note also the unphysical vortex decay when the downstream plane is moved aft of the body, as highlighted in the upper box: 4 to 10 power counts reduction over 3 chords depending on the grid density. As we consider an inviscid flow, there should be no viscous dissipation and therefore the transverse kinetic energy should be convected by the flow. This numerical dissipation is the reason why the downstream plane is located as close as possible to the body to get the results of Table 4.

4.5. Discussion

From a momentum perspective, the generation of vortex is seen as a loss and therefore as (lift-induced) drag. From the energy (exergy) standpoint on the other hand, the reversible formation of vortices is seen a potential for work generation, *i.e.* a beneficial phenomenon, which is a radically new perspective. The potential for energy recovering is not new but the exergy analysis appears to provide the rigorous formalism to determine the sources of design improvement in any flow field.

5. 3D NACA0012 WING – RANS

This test case has been chosen to investigate all flow phenomena of interest for an unpowered configuration in a unique computation: viscous phenomena, shock waves and vortices.

5.1. Grid & Numerics

The geometry consists in a rectangular wing of span length 4 and based on a NACA 0012 profile of unit length. The grid is made up of two symmetrical blocks as illustrated in Fig. 10 and contains a total 1.2 millions nodes. The grid extends 30 chords in all directions and provides a y^+ lower to unity. Note that only one mesh density has been generated.

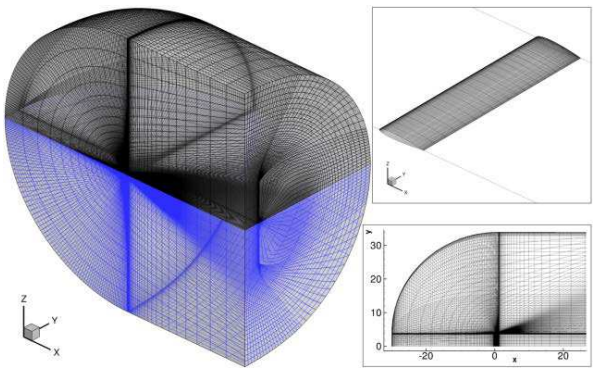

Figure 10 : 3D grid of the NACA 0012-based wing

A transonic flow at M_∞ = 0.75, Re = 2.6 10^6 and 3 degrees incidence has been computed and is analysed next.

5.2. Flow Visualisation

Fig. 11 gives an overview of the flow around the wing. Red contours highlight the anergy generation by viscous dissipation and thermal mixing while *Mach* isolines indicate the chordwise location of the shock.

The dissipation occurring in the wake and within the boundary layers is clearly made visible by the contours of viscous dissipation (first slice and wake) and, in a lesser extent, by thermal mixing (second slice).

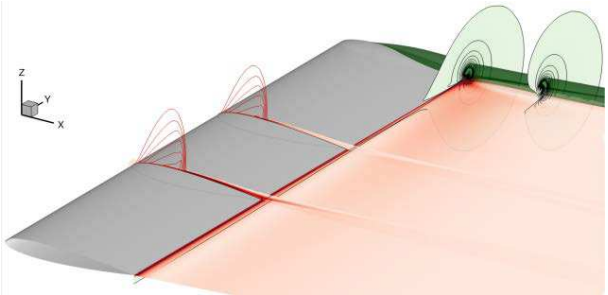

Figure 11 : 3D Wing immersed in a transonic RANS flow solution. Contours of anergy and transverse kinetic energy.

Fig. 12 illustrates the contributions to the main outflows across the downstream plane.

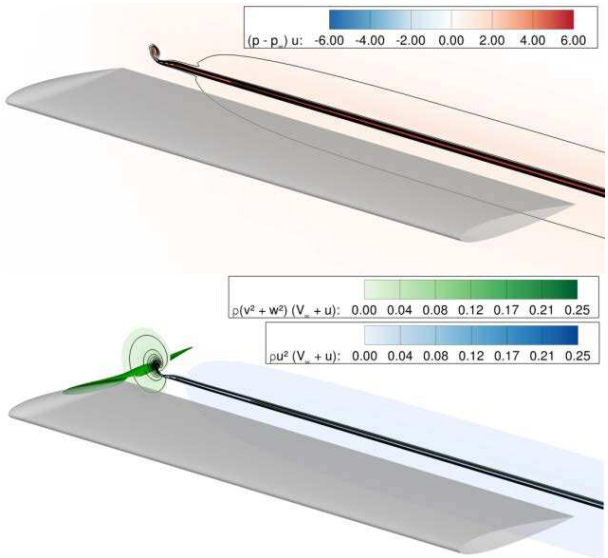

Figure 12 : 3D Wing immersed in a transonic RANS flow solution. Contours of mechanical energy outflows.

$\dot{E}_p$ and $\dot{E}_u$ are clearly associated to the wake while $\dot{E}_v$ is evidently associated to the lift-induced vortex, as expected.

5.3. Performance Prediction

Tables 5 presents the results for the near-field and far-field drag approaches while Table 6 gives those of the exergy-based formulation when the plane is located 0.25 root chord downstream.

Note the good agreement between the near-field and the far-field drag approaches, suggesting a satisfactory flow solution.
Again, the direct method provides a wave anergy close to the far-field drag approach while the indirect method overestimates this term but yields a total in close agreement to the drag approaches. A non-negligible thermal exergy is observed and mainly due to the compressibility of the flow.

Finally note that the sum of the mechanical energy outflows gives $C\dot{E}_{tot} = 44.70$ pc which is close to the lift-induced drag calculated by the far-field approach.

5.4. Wake Analysis

Fig. 13 represents the chordwise generation of anergy in the vicinity of the wing. The anergies associated to viscous dissipation and thermal mixing are given in green and pink respectively; their sum is the blue line. The total anergy outflow (including wave anergy) is represented in orange.

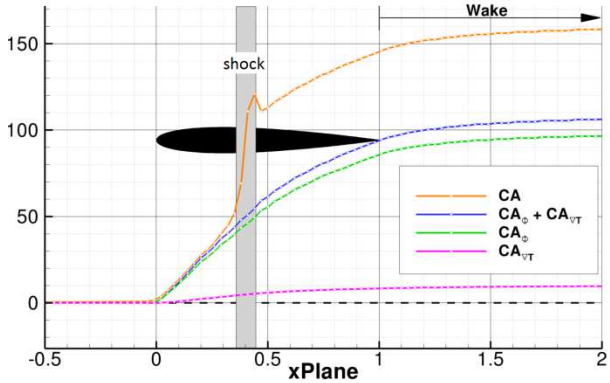

Figure 13 : 3D Wing immersed in a transonic RANS flow solution. Chordwise anergy generation.

First note the smooth and continuous increase in the volume terms $\dot{A}_\Phi$ and $\dot{A}_{\nabla T}$, effectively starting at the leading edge. On the other hand, the total anergy exhibits clearly the location of the shock (x≈0.4).
The anergy generated up to the trailing edge is roughly equal to 150 *pc* over a total of slightly more than 200, meaning that the wake dissipation represents about 25% of the loss generation.

Fig. 14 represents the chordwise change in the axial and transverse kinetic outflows in blue and green respectively as well as the boundary pressure-work rate in orange.

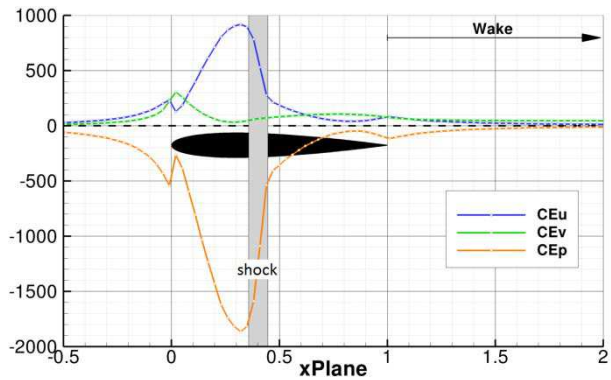

Figure 14: 3D Wing immersed in a transonic RANS flow solution. Chordwise mechanical outflows variation.

In front of the leading edge, the flow velocity has been converted into pressure ($p > p_\infty$) and, as u is negative, so is $\dot{E}_p$. Starting from the leading edge, one can observe a dramatic increase in both $\dot{E}_u$ and $\dot{E}_p$ until the shock location whose process has effectively reduced the mechanical energy of the flow.

Fig. 15 illustrates all terms related to thermal exergy. The surroundings work is given in red, the thermal energy outflow in green, the total anergy outflow in orange and the thermal exergy in blue.

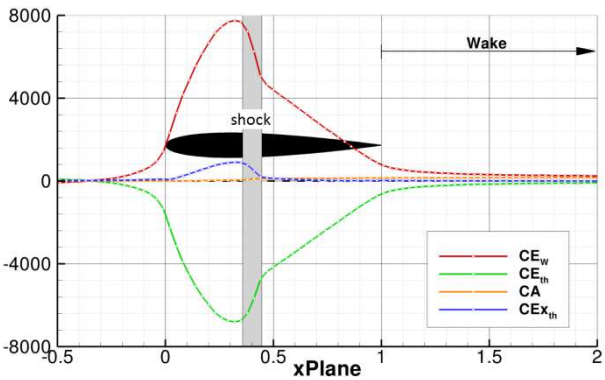

Figure 15 : 3D Wing immersed in a transonic RANS flow solution. Chordwise thermal exergy variation.

From the leading edge to the shock, the fluid expands and therefore the system pushes the atmospheric air which is observed in the surroundings work $\dot{E}_W$. As a result of the expansion, the thermal energy of the fluid is reduced, see $\dot{E}_{th}$. Across the shock wave that rapidly compresses the fluid, the temperature is dramatically increased, as expected.
The overall change in thermal exergy is relatively small and mainly due to compressibility. Finally, thermal exergy rapidly tends towards zero downstream of the trailing edge.

CONCLUSION

A formulation for predicting the aerodynamic performance of unpowered configuration has been introduced. It is based on a thermodynamic approach that evaluates the destruction of exergy by irreversible phenomena. The derivation involves the conservation of mass and momentum as well as the first and second laws of thermodynamics.
The formulation has been numerically implemented in a fortran code. Validation of the formulation and verification of the code has been performed through the investigation of various 2D and 3D test cases. Comparison has been made to the traditional near-field approach and to a well-established far-field approach.
It has been found that approximations in the computation of velocity gradients (and temperature gradients in a lesser extent) are likely to be source of the discrepancy observed for coarse meshes. For medium to fine grids, acceptable results are obtained, *i.e.* within one drag count of the near-field drag coefficient. Alternative ways of computing the gradients are currently under study to improve the aerodynamic performance prediction.
Focus has additionally been put on the numerical calculation of the term associated to the shock waves. Two methods have been introduced and compared. First, a direct method relying on the definition of a surface enclosing the shock provides a higher precision on coarse meshes but is not able to compensate the weakness of the gradients calculation. On the other hand, an indirect method relying on the divergence theorem overestimates the wave term and, as a result, yields a total drag-power in good agreement with the near-field approach. Both methods seem to converge on fine meshes, in agreement with their theoretical equivalence.

By redefining the aerodynamic losses as irreversible phenomena, the exergy-approach yields a new point of view, especially concerning lift-induced vortices. Contrary to a momentum analysis which would conclude that the generation of vortices is a loss of momentum, and therefore an undesirable phenomena, the exergy analysis concludes that the transverse kinetic energy associated represents a potential for work extraction. The generation of vortices can be valued through wing-tip turbines or flight formation for example.

Despite the current lack of accuracy that has been identified for coarse grids, the formulation and its implementation are considered capable of accurately assessing aerodynamic performance of three-dimensional lifting bodies immersed in transonic flows. The next step in the development process is the investigation of more complex configurations including propulsion systems.

1. Felder, J. J., Brown, G. V., Kim, H.D. & Chu, J. (2011). “Turboelectric Distributed Propulsion in a Hybrid Wing Body Aircraft”, 20th ISABE Conference, 12-16 September, Gothenburg, Sweden.

2. Cambier, L., Heib, S. & Plot, S., (2013). ``The Onera elsA CFD Software: Input from

Research and Feedback from Industry," *Mechanics & Industry*, **14**(3), 159-174.

3. Tognaccini, R. (2003). "Methods for Drag Decomposition, Thrust-Drag Bookkeeping from CFD Calculations", VKI Lecture Series 2003: CFD-based Aircraft Drag Prediction and Reduction, Rhode Saint Genèse, 3-7 February.

4. Destarac, D. (2003). "Far-Field / Near-Field Drag Balance and Applications of Drag Extraction in CFD", VKI Lecture Series 2003: CFD-based Aircraft Drag Prediction and Reduction, Rhode Saint Genèse, 3-7 February.

NC	$C\dot{E}_{tot}$	$C\dot{\mathfrak{E}}_{th}$	$C\dot{A}_{\Phi}$	$C\dot{A}_{\nabla T}$	CD_{ε}	CD_{f}	CD_{p}	CD_{nf}	CD_{ff}
256	3.01	0.05	83.40	0.46	**86.91**	74.59	15.81	**90.40**	**90.10**
512	2.95	0.05	86.02	0.48	**89.49**	75.19	15.21	**90.40**	**90.41**
1024	2.84	0.04	86.70	0.49	**90.08**	75.36	15.03	**90.39**	**90.41**
2048	2.81	0.04	86.79	0.49	**90.13**	75.33	14.97	**90.29**	**90.30**

Table 1: 2D NACA 0012 Airfoil immersed in a fully turbulent flow at zero incidence, M_{∞} = 0.20 and Re = 3 10^6. Mesh refinement study with comparison to the near-field and far-field drag approaches. Terms expressed in drag counts or power counts for a plane located 2 chords downstream of the body.

NC	CD_{f}	CD_{p}	CD_{nf}	CD_{v}	CD_{w}	CD_{ff}	CD_{sp}
256	62.19	110.05	**172.24**	115.98	53.83	**169.82**	2.43
512	62.89	106.24	**169.13**	112.43	55.87	**168.30**	0.83
1024	63.02	105.40	**168.42**	111.44	56.64	**168.08**	0.34
2048	63.01	105.20	**168.20**	111.11	57.10	**168.21**	0.00

Table 2: 2D NACA 0012 Airfoil immersed in a fully turbulent flow at zero incidence, M_{∞} = 0.80 and Re = 3 10^6. Mesh refinement study for the near-field and far-field drag approaches. Terms expressed in drag counts.

NC	$C\dot{E}_{tot}$	$C\dot{\mathfrak{E}}_{th}$	$C\dot{A}_{\Phi}$	$C\dot{A}_{\nabla T}$	$C\dot{A}_{v}$	$C\dot{A}_{w}^{d}$	CD_{ε}	$C\dot{A}_{w}^{i}$	CD_{ε}
256	3.94	1.29	96.25	11.20	112.68	51.13	**163.81**	59.34	**172.02**
512	3.78	1.34	95.69	11.19	112.01	55.60	**167.61**	57.20	**169.21**
1024	3.78	1.32	95.35	11.17	111.62	55.63	**167.25**	56.80	**168.42**
2048	3.84	1.32	95.20	11.17	111.53	56.43	**167.96**	56.70	**168.23**

Table 3: 2D NACA 0012 Airfoil immersed in a fully turbulent flow at zero incidence, M_{∞} = 0.80 and Re = 3 10^6. Mesh refinement study for the exergy-based formulation. Terms expressed in power counts for a plane located 2 chords downstream of the body.

NC	$C\dot{E}_{u}$	$C\dot{E}_{v}$	$C\dot{E}_{p}$	$C\dot{\mathfrak{E}}_{th}$	CD_{ε}	CD_{nf}	CD_{ff}	CD_{sp}	CD_{ref}
64	41.25	134.07	-76.46	1.41	**100.27**	**157.01**	**100.28**	56.73	**101.64**
128	38.61	137.72	-75.79	1.44	**101.98**	**119.54**	**103.03**	16.51	**103.59**
256	37.98	139.57	-75.71	1.46	**103.31**	**108.27**	**104.14**	4.13	**104.22**

Table 4: 3D wing theoretically elliptically loaded immersed in an inviscid, calorically perfect and low-speed flow (M_{∞} = 0.20) at 6 deg incidence. Mesh refinement study with comparison to the near-field and far-field drag approaches.

CD_{f}	CD_{p}	CD_{nf}	CD_{v}	CD_{i}	CD_{w}	CD_{ff}	CD_{sp}
64.95	144.17	**209.12**	116.06	45.58	47.48	**209.11**	0.01

Table 5: 3D NACA0012-type wing immersed in a fully turbulent flow at 3 deg incidence, M_{∞} = 0.75 and Re = 3 10^6. Results of the near-field and far-field drag approaches. Terms expressed in drag counts.

$C\dot{E}_{u}$	$C\dot{E}_{v}$	$C\dot{E}_{p}$	$C\dot{\mathfrak{E}}_{th}$	$C\dot{A}_{\Phi}$	$C\dot{A}_{\nabla T}$	$C\dot{A}_{w}^{d}$	CD_{ε}	$C\dot{A}_{w}^{i}$	CD_{ε}
41.12	53.46	-49.88	12.57	91.61	8.87	46.70	**204.45**	51.91	**209.66**

Table 6: 3D NACA0012-type wing immersed in a fully turbulent flow at 3 deg incidence, M_{∞} = 0.75 and Re = 3 10^6. Results of the exergy-based formulation. Terms expressed in power counts for a plane located 0.25 root chord downstream of the body.